Journal of the Brazilian Society of Mechanical Sciences and Engineering (2020) 42:171
https://doi.org/10.1007/s40430-020-2229-2

TECHNICAL PAPER

Experimental and numerical study of laminar separation bubble formation on low Reynolds number airfoil with leading-edge tubercles

B. K. Sreejith[1] · A. Sathyabhama[2]

Received: 5 February 2019 / Accepted: 12 February 2020

Abstract

The present work reports the effect of leading-edge tubercles on aerodynamic performance and flow features of a cambered airfoil E216 at a Reynolds number of 100,000 and at various angles of attack in the pre-stall regime. Amplitude values of 2 mm, 4 mm and 8 mm and wavelength values of 15.5 mm, 31 mm and 62 mm are used for both experimental and simulation studies. The Transition-SST RANS model is used to simulate transition phenomenon (laminar separation bubble) and three-dimensional flow features over the airfoil. Wind tunnel experimental results are used for the performance analysis and the validation of the simulation methodology. The experimental values of C_l and C_d are 1.37 and 0.081, respectively, at a stall angle of 12° for the plain airfoil. The experimental results show that the lift generated by tubercled airfoils is higher than that produced by the plain airfoil in the pre-stall region but lower at the stall angle. A maximum benefit of 4.51% in C_l is obtained for the tubercled airfoil with the highest amplitude (8 mm) and wavelength (64 mm) at 6° angle of attack. A higher C_d is observed for all the tubercled airfoils than for the plain one. The simulation is mainly carried out to study the flow structure. Simulation results indicate the presence of laminar separation bubbles on the plain airfoil with a straight separation and reattachment line parallel to the trailing edge. The tubercles considerably altered the laminar separation bubble formation and the flow structure. A sinusoidal laminar separation bubble is formed on the tubercled airfoils with reduced bubble length. The laminar separation bubble along the trough is formed ahead of that at peak. Two pairs of counter-rotating vortices are formed on the airfoil surface along the trough at two different chord-wise locations which strongly alter the flow pattern over it. Prandtl's secondary flow of the first kind is the key reason for the vortex formation.

Keywords Airfoil · Laminar separation bubble · Tubercle · Turbulent flow · Vorticity

List of symbols

c	Chord length (m)
C_p	pressure coefficient
C_d	Drag coefficient
C_l	Lift coefficient
k	Turbulent kinetic energy (m^2/s^2)
Re	Reynold number based on chord length
Re_θ	Momentum thickness Reynolds number
$Re_{\theta c}$	Critical Reynolds number
$Re_{\theta t}$	Momentum thickness Reynolds number
$\tilde{Re}_{\theta t}$	Local transition onset momentum thickness Reynolds number
Re_v	Strain rate (vorticity) Reynolds number
Re_ν	Viscosity ratio Reynolds number
S	Strain rate
x/c	Axial distance over airfoil along axial chord
y^+	Non-dimensional wall distance

Greek symbols

α	Angle of attack (°)
γ	Intermittency
δ^*	Boundary layer displacement thickness (m)
μ_t	Eddy viscosity (m^2/s)
μ	Molecular viscosity (Pa s)
Ω	Absolute value of vorticity
ρ	Density (kg/m^3)

Technical Editor: Francis HR Franca, Ph.D.

✉ B. K. Sreejith
srijithbk@gmail.com

A. Sathyabhama
bhama72@gmail.com

[1] Department of Mechanical Engineering, AJ Institute of Engineering and Technology (Affiliated to Visvesvarya Technical University, Belgaum, Karnataka), Mangalore 575 006, Karnataka, India

[2] Department of Mechanical Engineering, National Institute of Technology Karnataka, Surathkal, Mangalore 575 025, India

Published online: 14 March 2020

ω	Specific turbulence dissipation rate (s^{-1})
θ	The boundary layer momentum thickness (m)

Suffix

∞	Free stream entity
$_0$	Static entity
t	Transition onset
s	Streamline

Abbreviations

AOA	Angle of attack
CFD	Computational fluid dynamics
LSB	Laminar separation bubble
3D	Three dimensional
RANS	Reynolds averaged Navier–Stokes
Re	Reynolds number
SIMPLE	Semi-implicit method for pressure-linked equations
SSWT	Small-scale wind turbine
TKE	Turbulent kinetic energy

1 Introduction

Tubercles are the leading-edge undulations incorporated on an airfoil as a passive flow control technique [1]. The tubercles considerably alter the pre-stall and post-stall aerodynamic performance of the airfoils. A performance improvement of 6% in maximum lift without drag increment was obtained in a study by Miklosovic et al. [17] at lower angles of attack. In contrast, Hansen et al. [12] reported drag increment and performance reduction in the pre-stall region. Similarly, Johari et al. [14] observed reduced performance in the pre-stall region and lift improvement without any increase in drag in post-stall. The stall angle and the maximum lift coefficient were reduced with a significant increase in drag compared to the airfoil without tubercles. In a similar study, Corsini et al. [5] reported a 30% lift improvement in the post-stall region, but the study lacks explanation regarding the flow mechanism. Cai et al. [2] numerically studied the effect of single protuberance on NACA $63_0 - 23$ airfoil using the Spalart-Allmaras turbulence model. They observed a mild decline in the coefficient of lift (C_l) near the stall region, and reduced stall angle and improved performance near the post-stall region. They concluded that even a single protuberance can significantly alter the airfoil performance.

Several attempts have been done to explain the reason behind the difference in the performance of airfoil with tubercles and plain airfoils. Hansen [11] compared the effects of tubercles on the performance of two different airfoils (NACA 0021 and NACA 65-021) and reported that a pair of counter vortices between the peak of the tubercles promote flow modification along the stream-wise direction. It was suggested that the tubercles act as vortex generators which cause stall delay. Custodio [6] observed similar stream-wise counter-rotating vortices and proposed that these vortices are the cause for the enhanced performance of airfoil at high angle of attack (AOA). Pedro and Kobayashi [18] and Fish and Battle [8] reported similar results and proposed that these vortices enhance the boundary layer mixing and carry momentum to the boundary layer, which delays the separation. Tubercles generate wall-normal (transverse) three-dimensional vortices that move in the stream-wise direction [26]. Favier et al. [7] reported in their DNS study that a Kelvin–Helmholtz-like instability driven by the span-wise modulation of the stream-wise velocity profile induced by the tubercles is the reason for the generation of the stream-wise vortices and it controls the boundary layer separation.

Skillen et al. [24] suggested that the tubercles induce a secondary-flow mechanism that enhances momentum transfer and reduces flow separation in the transition region. A similar mechanism was also proposed by Rostamzadeh et al. [20] called Prandtl's secondary flow of the first kind where tubercles reorganise span-wise vorticity into stream-wise and transverse vorticity. There are contradictory opinions about the flow mechanism that is responsible for the improved performance of the airfoil with tubercles. Van Nierop et al. [27] proposed that when the wavelength and amplitude of tubercles are larger than the boundary layer thickness, tubercles cannot act as a vortex generator. They demonstrated that the bumps of the tubercles alter the pressure distribution on the wing such that separation of the boundary layer was delayed behind the bumps, which ultimately lead to a gradual onset of stall and a larger stall angle.

The boundary layer around an airfoil must negotiate areas of favourable and adverse pressure gradients (APG). A favourable pressure gradient is one in which the pressure is decreasing in the direction of the flow and is present on the leading-edge portion of the airfoil. As the curvature of the surface changes sign, the static pressure increases with downstream distance thus creating an APG. At some point, portions of the flow very near the surface of the airfoil begin to move in a direction opposite to that of the free stream. This point is the separation point of the boundary layer. At low Reynolds numbers (Re), the free stream laminar flow contains very little kinetic energy and is not able to overcome the APG and usually separates from the airfoil surface. The separated laminar boundary layer from the airfoil surface transitions to turbulent flow and gains energy due to momentum exchange with the mean flow. If enough energy is gained by the turbulent flow, the boundary layer will be able to withstand the APG and subsequently reattach to the surface [28] as shown in Fig. 1. The region between the flow separation and reattachment forms a recirculating dead air zone and is called laminar separation (LSB) [13].

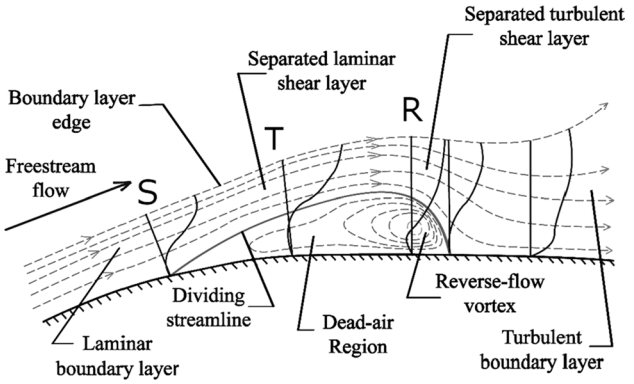

Fig. 1 Laminar separation bubble—zoomed view [28]

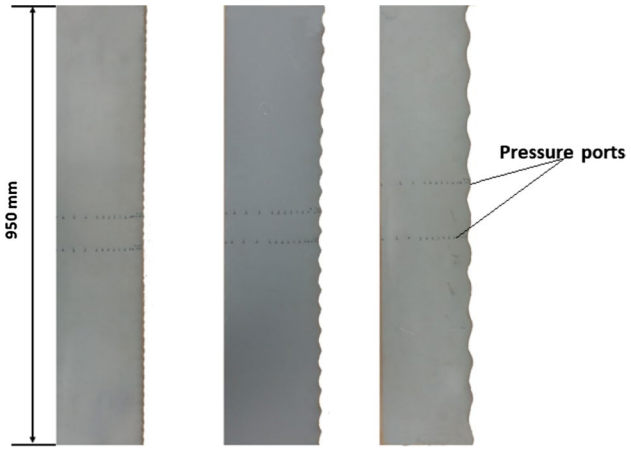

Fig. 2 Tubercled airfoils used for experiment: **a** A2W15.5, **b** A4W31 and **c** A8W62

This region of LSB induces additional thickness and pseudo camber on the airfoil. It results in a performance reduction of the airfoil. Controlling the LSB involves the use of vortex generators, which promote the premature conversion of laminar flow to turbulent flow. Boundary layer grits, boundary layer wires, boundary layer trips (BLT) and surface dimples [19] are some of the passive flow control techniques used with the aim of controlling LSB. Any geometrical modification (such as tubercles) may have significant effects on the flow field and LSB formation. Currently, the majority of studies have considered only thick, symmetric foils and wings as they approximate Humpback whale flippers. The effect of tubercles on thin and highly cambered airfoils such as E216 are less reported. Moreover, the effect of tubercles on LSB formation is still to be explored.

The present work involves the experimental and numerical study of the performance of a low-Re airfoil E216 with leading-edge tubercles in the pre-stall region at $\mathrm{Re} = 100,000$. The study mainly focuses on the effect of tubercles on the LSB formation and the related flow structure. The steady-state SST-Transition model is used as the turbulence model in the numerical scheme, and the simulation is carried out using ANSYS 15.0.

2 Experimental and measurement techniques

2.1 Geometry

The E216 airfoil is employed as the geometry cross-sectional profile for both plain and tubercled airfoils. It exhibits good aerodynamic performance at low Re, which makes it a good candidate for small-scale wind turbine (SSWT) blades [25]. Three types of tubercle configurations, A2W15.5, A4W31 and A8W62, are studied in the present work (Fig. 2), where A is the amplitude and W is the wavelength of the tubercle. The detailed nomenclature is shown in Fig. 3. The tubercled airfoil names are given as '$A(x)W(y)$' where 'x' and 'y' represent the corresponding amplitude and wavelength in mm. The same airfoil shape (E216) is maintained throughout the span by scaling it from peak to trough without any profile change. The values used here for the amplitude and wavelength are based on the data of an actual whale flipper [8]. The airfoils have chord length (c) of 150 mm with span of

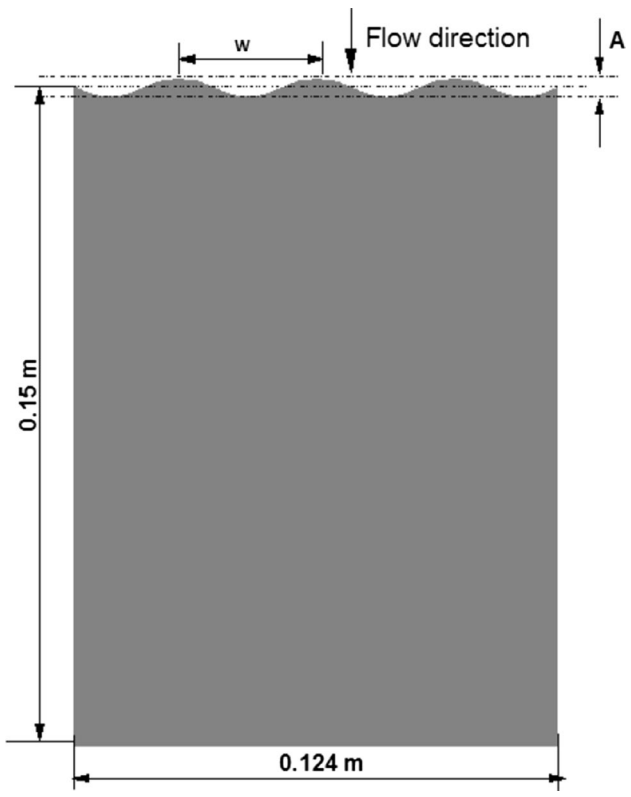

Fig. 3 Tubercled airfoil showing the nomenclature and dimensions used for simulation

950 mm for experiment and 124 mm for simulation. The airfoils used for the experimental study are shown in Fig. 2. The pressure taps are located near the midspan of the test airfoils. For the plain airfoil, a total of 28 pressure taps are laid, 19 on the suction side and 9 on the pressure side. The location of these pressure ports is the same for the tubercled airfoils, but in this case, two such rows of pressure ports, one along the crest and other along the trough, are provided. The ports are unevenly spaced with a greater number of them towards the leading-edge. Stainless tubes of 0.50 mm inner diameter are internally connected to these pressure ports and the pressure is sensed with an electronic manometer.

Experiments are conducted in a subsonic open wind tunnel facility in the Mechanical Engineering Department of the National Institute of Technology Karnataka, India. The tunnel has a 1 m × 1 m square-shaped cross section and length of 2m with maximum airflow speed of 35 m/s. The tunnel is of suction type with an empty test section turbulence level less than 0.12% over the tunnel operating range. Surface pressure measurement is used for the C_l determination and a wake survey using a pitot tube is adopted for C_d measurement. The Pitot tube is mounted at 1.5c downstream of the airfoil to measure the wake created by the airfoil in the flow. The pitot tube is attached to a manually operated vertical traverse system. The pitot tube is lowered by 5 mm spatial increments starting from 3c above to 3c below the centre of the tunnel. Loss in momentum in the flow behind the airfoil in terms of momentum thickness is used to calculate the coefficient of drag (C_d) of the airfoil.

Pressure measurements are done using the HTC-made PM-6202 model electronic differential manometer. The measurement range of this manometer is ± 2 psi with an accuracy of ± 0.3%. One end of the manometer is connected to the pressure port in the airfoil and the other end is open to the atmosphere. Experiments are conducted on the plain airfoil and tubercled airfoil at AOAs of 0°–14° to quantify the aerodynamic performance in the pre-stall range and just after the stall. The study is conducted at the Re of 100,000.

The maximum blockage created by the airfoil inside the tunnel is less than 5% and hence blockage corrections are not required [3]. The uncertainty of the electronic manometer used in the experiment for measuring pressure is ± 0.03%. The uncertainty in the derived quantities is calculated as explained in reference [15], and its values are given in Table 1.

Table 1 Uncertainty in derived quantities

Quantity	% uncertainty
C_p	± 0.31
Velocity	± 0.43
Re	± 0.58
C_l	± 0.79
C_d	± 0.21

3 Numerical methodology

3.1 Geometry

The tubercled airfoils A2W15.5, A4W31 and A8W62 are used for the simulation in the present work and are shown in Fig. 4.

3.2 Computational domain and mesh

The three-dimensional rectangular computational domain is created using ICEM CFD of ANSYS 15.0 as shown in Fig. 5. The total length of the computational domain is set to 25 times the chord length (c), 9c in front of the airfoil in order to achieve fully developed flow, 15c behind the airfoil, and a height of 20c to avoid any wall effect. The width of the domain is set to 0.83c to cover in the span-wise direction flow over a pair of peaks of the tubercle considering the highest wavelength of 62mm. The three-dimensional, structured mesh is also created using ICEM CFD. A high-resolution mesh is created in the region close to the airfoil where greater computational accuracy is needed and is shown in Fig. 6 and 7. As per the requirements of the turbulent model used, the height of the first cell adjacent to the surface is set such that it results in a y^+ value lower than one.

The boundary conditions used are as follows: (1) Velocity inlet at the inlet to the domain, top and bottom boundaries (2) pressure outlet at the outlet of the domain (3) No slip on the airfoil surface and (4) symmetry at side walls. The symmetry boundary condition mirrors the geometry and flow characteristics in the span-wise direction, approximating the computational model of the wing to the full span length of the experimental configuration. The free stream temperature is set to 308 K, the same as the ambient temperature in which the experiments were carried out, and the other required properties of the fluid are calculated accordingly. For the Re of 100,000 and airfoil chord length of 150 mm, the free stream inlet velocity of air is calculated to be 10.08 m/s. The flow is considered as steady and incompressible. To solve the momentum equations, the semi-implicit method for pressure-linked equations (SIMPLE) algorithm [9] and a second-order upwind spatial discretisation are employed in the calculations. The least square cell-based method is set for spatial gradient. A Residual target value of 10^{-6} is set as a convergence criterion for all transported scalars.

3.3 Turbulence model

A numerical model which can capture transition phenomenon like LSB is required for the present work. The Langtry–Menter 4-equation Transitional SST Model or $\gamma - \mathrm{Re}_\theta$-SST model [16] has shown to be capable of capturing the natural transition

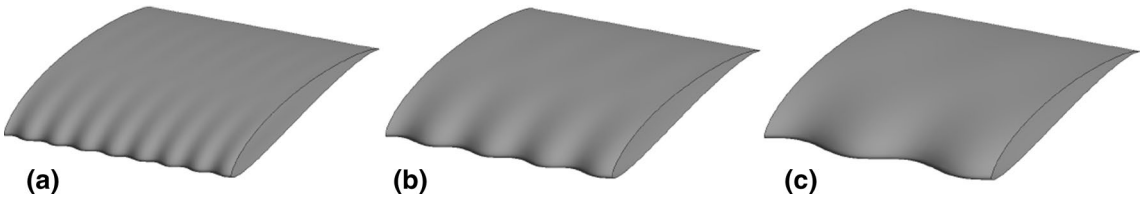

Fig. 4 Tubercled airfoils used for simulation: **a** A2W15.5, **b** A4W31 and **c** A8W62

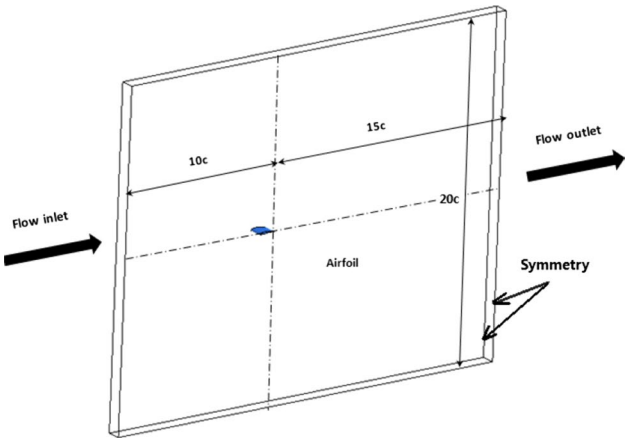

Fig. 5 Computational domain

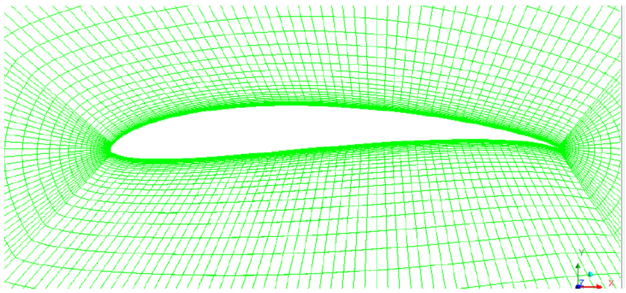

Fig. 6 Close view of dense grid nearer to the airfoil

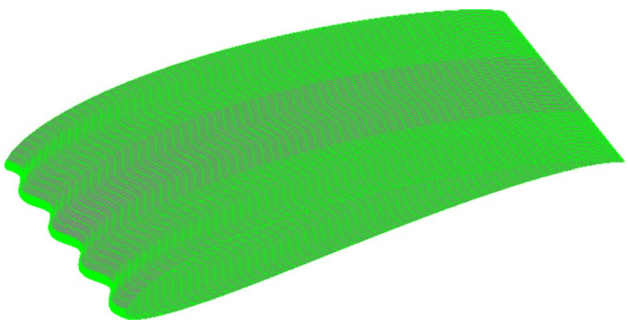

Fig. 7 Grid on the airfoil surface

phenomena. It is well-validated with many standard test data including airfoil test data. Chishty et al. [4] studied the effect of dimples in low pressure turbine cascade blades using Transitional SST Model and successfully modelled the separation and reattachment locations. Shah et al. [23] numerically simulated and studied the mechanism of the laminar separation bubble and the laminar-turbulent transition over the airfoil UBD5494 using the Transitional SST Model. Hence, the same model is used in the present work. The model is based on the two-equation $k-\omega$ SST model augmented by two additional equations, one for intermittency (γ) and another for transition onset momentum-thickness Reynolds number ($\tilde{\mathrm{Re}}_{\theta t}$), to describe the laminar-turbulent transition process. The intermittency term is employed to activate the production term of the turbulent kinetic energy (TKE) downstream of the transition point in the boundary layer, and the transition onset momentum-thickness Reynolds number term captures the non-local effect of the turbulence intensity. The governing equations involved in this analysis are listed below [9, 16, 23]. The turbulence kinetic energy, k, and the specific dissipation rate, ω, are obtained from the following transport equations:

$$\frac{\partial(\rho k)}{\partial t}+\frac{\partial(\rho u_i k)}{\partial x_i}=\frac{\partial}{\partial x_j}\left[\left(\Gamma_k\frac{\partial k}{\partial x_j}\right)\right]+G_k-Y_k+S_k \tag{1}$$

and

$$\frac{\partial(\rho\omega)}{\partial t}+\frac{\partial(\rho u_i \omega)}{\partial x_i}=\frac{\partial}{\partial x_j}\left[\left(\Gamma_\omega\frac{\partial \omega}{\partial x_j}\right)\right]+G_\omega-Y_\omega+S_\omega \tag{2}$$

In these equations, G_k represents the generation of turbulence kinetic energy due to mean velocity gradients. The G_ω represents the generation of ω. The Γ_k and Γ_ω represent the effective diffusivity of k and ω respectively. The Y_k and Y_ω represent the dissipation of k and ω due to turbulence. The S_k and S_ω are user-defined source terms.

The following transport equation is solved to calculate the value of the intermittency term, γ.

$$\frac{\partial(\rho\gamma)}{\partial t}+\frac{\partial(\rho U_j\gamma)}{\partial x_j}=P_{\gamma1}-E_{\gamma1}+P_{\gamma2}-E_{\gamma2}+\frac{\partial}{\partial x_j}\left[\left(\mu+\frac{\mu_t}{\sigma_\gamma}\right)\frac{\partial\gamma}{\partial x_j}\right] \tag{3}$$

where $P_{\gamma 1}$, and $E\gamma 1$ are the transition source terms. The value of constants used in the intermittency equations are $c_{\gamma 1} = 0.06$; $c_{e2} = 50$; $c_{\gamma 3} = 0.5$ and $\sigma_{\gamma} = 1.0$.

The local transition onset momentum thickness Reynolds number, $\tilde{Re}_{\theta t}$, is determined by solving the following transport equation:

$$\frac{\partial(\rho \tilde{\mathrm{Re}}_{\theta t})}{\partial t} + \frac{\partial(\rho U_j \tilde{\mathrm{Re}}_{\theta t})}{\partial x_j} = P_{\theta t} + \frac{\partial}{\partial x_j}\left[\sigma_{\theta t}(\mu + \mu_t)\frac{\partial \tilde{\mathrm{Re}}_{\theta t}}{\partial x_j}\right] \tag{4}$$

where $P_{\theta t}$ is the blending function used to turn off the source term in the boundary layer. The values of constants in the empirical relations in the original models are generated from the flat plate experiment. In order to get reliable solutions values of 0.02 and 3.0 are used for the constants, $c_{\theta t}$ and $\sigma_{\theta t}$, respectively, instead of the respective default values of 0.03 and 2.0 [23]. The tubercled values are based on low Re simulations of circular arc airfoils with which more physically realistic solutions were achieved which showed good agreement with experimental data.

3.3.1 Separation-induced transition correction

The model without the correction predicts the turbulent reattachment location far downstream compared to experimental results [16]. This is because the turbulent kinetic energy (TKE), k, in the separating shear layer is smaller at lower free stream turbulence intensities. As a result, it takes longer for the TKE to grow to large enough values that would cause the boundary layer to reattach. To correct this deficiency, a modification to the transition model is introduced that allows the TKE to grow rapidly once the laminar boundary layer separates. Separation-induced transition can be rewritten as,

$$\gamma_{\mathrm{sep}} = \min\left[2\max\left[\left(\frac{\mathrm{Re_v}}{3.235\mathrm{Re}_{\theta c}}\right) - 1, 0\right]F_{\mathrm{reattach}}, 2\right]F_{\theta t} \tag{5}$$

where

$$F_{\mathrm{reattch}} = \mathrm{e}^{-\left(\frac{R_T}{20}\right)^4} \tag{6}$$

and

$$\gamma_{\mathrm{eff}} = \max(\gamma, \gamma_{\mathrm{sep}}) \tag{7}$$

3.3.2 Coupling the transition model with SST transport equations

The transition model interacts with the SST turbulence model as below:

$$\frac{\partial(\rho k)}{\partial t} + \frac{\partial(\rho u_i k)}{\partial x_i} = \frac{\partial}{\partial x_i}\left(\Gamma_k \frac{\partial k}{\partial x_j}\right) + G_k^* - Y_k^* + S_k \tag{8}$$

where

$$Y_k^* = \min(\max(\gamma_{eff}, 0.1), 1.0)Y_k \tag{9}$$

and

$$G_k^* = \gamma_{\mathrm{eff}} G_k \tag{10}$$

where Y_k and G_k are the terms representing original destruction and production respectively for the SST model. The production term in the ω-equation is used without any modification.

3.4 Grid sensitivity study

To ensure the results are independent of the grid size, the grid number is increased until a negligible difference in the converged solution is attained. The methodology of optimum grid selection is adapted from [22]. Five different meshes are prepared for the grid independence study with a number of grid cells ranging from 700,362 to 2,141,000. Initially, the mesh number is varied globally all around the domain. The fluctuation in C_l and C_d values beyond of 1,637,020 cells is small. Further, the focus of the grid sensitivity study is shifted to an area closer to the airfoil. The simulations are carried out for AOA of 6° and the results are shown in Fig. 8. The variation in C_l and C_d values after a grid number of 1,237,620 is negligible, so this configuration is chosen for further simulations. To ensure the reliability of mesh, The y^+ distribution over the airfoil surface is presented in Fig. 9. The value is coming around 1 and is in an acceptable range.

4 Results and discussion

4.1 Performance of the plain airfoil

Plain airfoil performance study is done in wind tunnel by varying the AOA from 0° to 14° and at Re of 100,000. Results show that the airfoil stalls at the AOA of 12° with $C_l = 1.37$ and $C_d = 0.081$. Since the wake survey method used for C_d measurement does not give reliable results beyond stall, the experimental measurement is limited up to stall angle. Plain airfoil experimental results are used as a benchmark for the simulation results validation and the results are plotted in Figs. 10 and 11. Up to 6° AOA, the predicted C_l from the simulation is lower than the experimental value and it is higher than the experimental value for AOA beyond 6°. The flow becomes unstable on the suction side of the airfoil when the AOA approaches the stall angle. This could be the reason

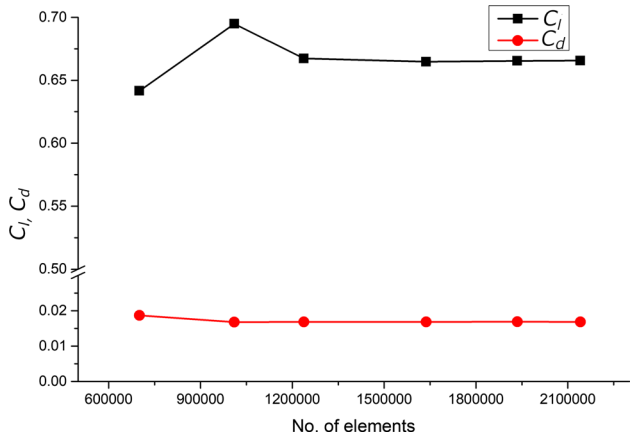

Fig. 8 Variation of C_l and C_d of the airfoil with grid number at AOA of 6°

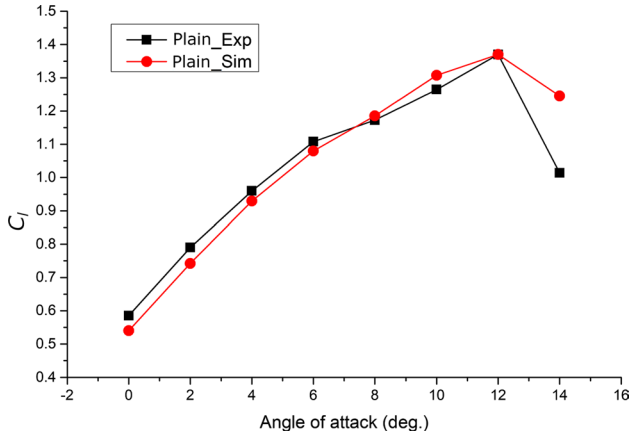

Fig. 10 Comparison of simulation and experimental C_l results for plain airfoil

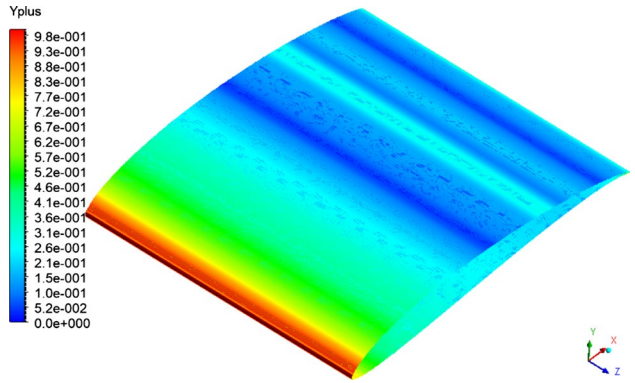

Fig. 9 y^+ distribution over airfoil surface

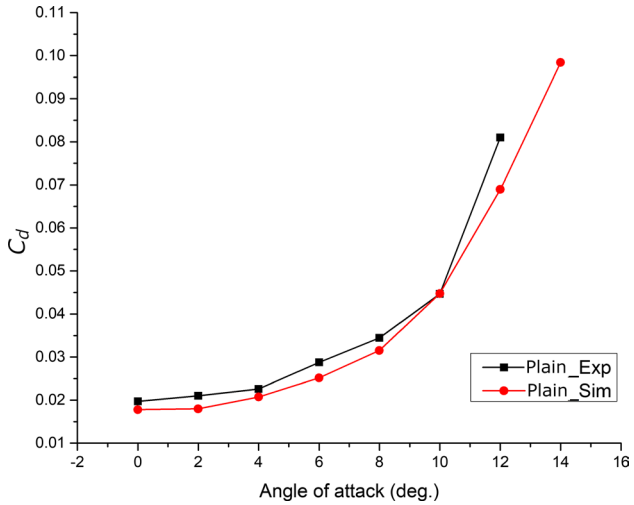

Fig. 11 Comparison of simulation and experimental C_d results for plain airfoil

for the sudden change in the slope of the experimental C_l curve beyond 6° AOA. There is a large deviation between experimental and simulation results after the stall angle of 12°, which may be due to the recirculation flow patterns that begin to shed at extreme angles. The numerical C_d prediction follows a similar trend as that of the experimental one but under-predicts the magnitude of the C_d as shown in Fig. 11. This is due to the difference in airfoil surface roughness in the simulation and experiment. Average deviations of 5.81% in C_l and 4.31% in the C_d between simulation and experimental results are observed. In the simulation, stall occurred at AOA of 12° with a C_l value of 1.37 and a C_d value of 0.069.

4.2 Airfoil with tubercles

4.2.1 Lift and drag coefficients

Figure 12 shows the wind tunnel experimental results for C_l of tubercled airfoils. It is observed that the effect of tubercles depends on the AOA. The result shows that for lower AOA (0° − 8°), all the tubercled airfoils have similar trend in C_l variation as that of plain airfoil results and the trend varies thereafter. Among the three tubercled airfoils, the tubercled airfoil with the highest amplitude and wavelength—A8W62, performs better than the plain airfoil until an AOA of 8°. With further increase in AOA its performance degrades. The tubercled airfoil has same stall angle as that of the plain airfoil (12°) but exhibits smoother stall properties. Maximum improvement of 4.51% in C_l is obtained at 6° and a reduction of 6.6% in C_l is observed at stall angle of 12° compared to the result of plain airfoil. The other tubercled airfoils have negligible improvement in C_l. All the tubercled airfoils exhibit smooth stall. The post-stall lift is lower than that of the plain airfoil except for A2W15.5.

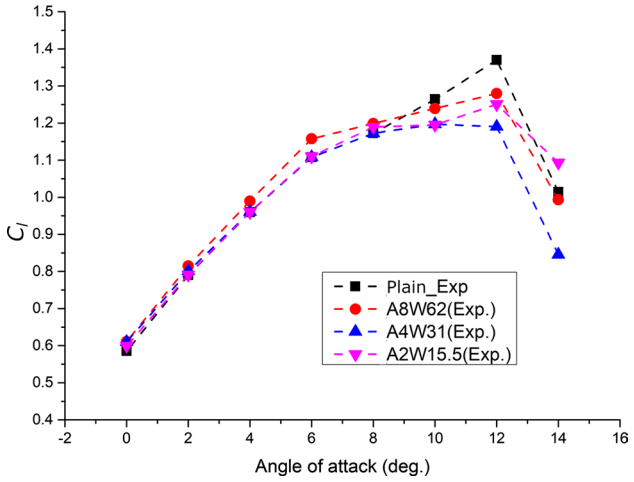

Fig. 12 Experimental results showing the effect of tubercles on C_l

The C_d of the tubercled airfoils obtained from the experiments and simulations are shown in Fig. 13. Experimental results show that all the tubercled airfoils generate higher C_d than the plain airfoil. The tubercled airfoil A4W31 exhibits the lowest C_d and A2W15.5 exhibits the highest C_d. The simulations yielded similar values and behaviours of the C_l and C_d curves as the experimental results.

To study the effect of tubercles on LSB formation as well as on the flow physics, the simulation results are analysed further as the experimental and flow visualisation facilities are limited.

4.2.2 Coefficient of pressure (C_p)

The presence and location of LSB on the airfoil can be identified from the coefficient of pressure (C_p) distribution [21]. The presence of LSB is evidenced by a plateau in the C_p distribution as shown in Fig. 14. The point on the pressure distribution that signifies the start of a pressure plateau indicates the point of separation. The transition point is located where the pressure plateau ends and the reattachment point corresponds to the location where the separated pressure distribution would cross the unseparated turbulent pressure distribution that would form on the airfoil at the same AOA. The region between the point of separation and point of reattachment represents LSB.

The C_p distribution over the suction and pressure surface of the tubercled airfoils along with that of the plain airfoil at an AOA of 4° obtained from the simulation study is presented in this section. For the plain airfoil, the C_p distribution is plotted along the midspan of the tubercled airfoil, and for the tubercled airfoils this distribution is plotted along two sections—one passing along the trough and one along the peak nearer to midspan. The upper surface of the airfoil has negative pressure and the lower surface has positive pressure. To give a realistic picture of the airfoil, the C_p axes are inverted here so that the upper curve represents the pressure on the upper surface and the bottom curve represents that on the lower surface.

The suction peak (highest magnitude of negative pressure) of -1.05 is observed for the plain airfoil near the leading-edge on the upper surface as shown in the figure. A pressure plateau is observed on the suction surface indicating the presence of LSB. The laminar boundary layer separates at around $x/c = 0.48$, represented by the starting point of pressure plateau, and subsequently reattaches at $x/c = 0.79$ resulting in a LSB length of 0.31c. (Fig. 15, plain airfoil curve).

For the tubercled airfoil A2W15.5, the magnitude and location of suction peak have not been significantly altered due to the presence of tubercles for the tubercle peak region (Fig. 15). However, for the trough region of the tubercle, an increase in peak suction pressure (− 1.18) is observed. Downstream the suction peak, the suction pressure behind

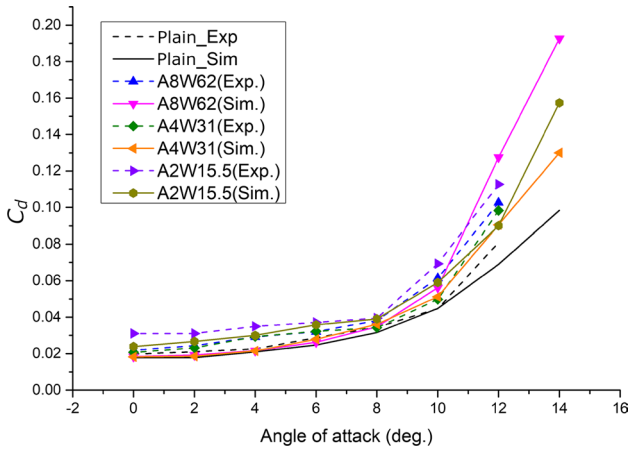

Fig. 13 Comparison of simulation and experimental results for C_d

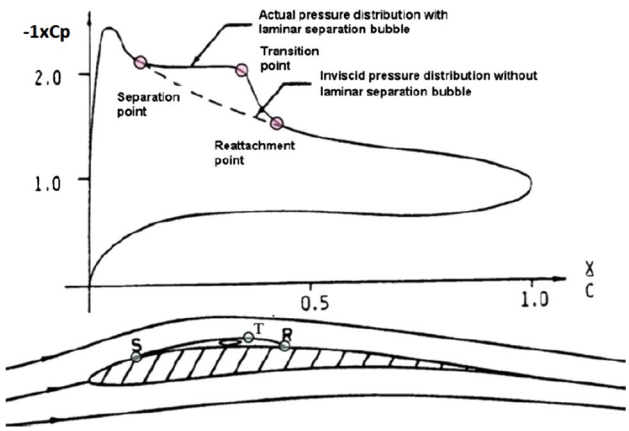

Fig. 14 Cp distribution over a typical airfoil [21]

the peak and trough regions coincide with that for the plain airfoil. A very weak LSB represented by a vague pressure plateau is formed close to trailing edge for both peak and trough regions of the tubercle. The flow starts to separate at 0.63c and reattaches at 0.92c resulting in a bubble size of 0.29c. The length of the bubble is reduced by 6.5% when compared to the plain airfoil. Peak suction pressure values for peak and trough regions of the tubercle are − 1.08 and − 1.24, respectively, for the tubercled airfoil A4W31 as shown in Fig. 16. The suction peak of plain airfoil lies in between these two values. In this case, stronger LSB is formed compared to A2W15.5. In both peak and trough, it is observed that the location of the LSB is different than the plain airfoil. Behind the trough, the flow separation starts at $x/c = 0.39$ and reattaches at $x/c = 0.63$ with a total bubble length of 0.24c. Along the peak, the LSB formation starts at around $x/c = 0.65$ and ends at $x/c = 0.87$, which results in total length of 0.22c. The strength of both the LSBs is lower with an average reduction in bubble length of 25.8% compared to the plain airfoil. The LSB along the trough occurs much upstream compared to that along the peak. This indicates the formation of the LSB in a wavy manner along the span-wise direction for the tubercled airfoil unlike the straight LSB in the case of the plain airfoil. In the case of tubercled airfoil, A8W62, the suction peak is reduced to − 1.04 for the tubercle peak and is increased to − 1.38 for the tubercle trough, as shown in Fig. 17. The separation behind trough starts at $x/c = 0.37$ and reattaches at $x/c = 0.58$, resulting in a LSB length of 0.21c, and for the peak starts at $x/c = 0.65$ and ends at $x/c = 0.90$, with total bubble length of 0.25c. The intensity of the LSB formation is comparatively less than the plain airfoil along trough, in addition to the reduction in length of the LSB. The LSB formed in a wavy shape with an average reduction in LSB length by 25.8%. For all the tubercled airfoils considered above, the surface pressure characteristics on the lower surface of the airfoil are almost similar to that of the plain airfoil. The details regarding the flow separation point, reattachment point, and bubble size are listed in Table 2.

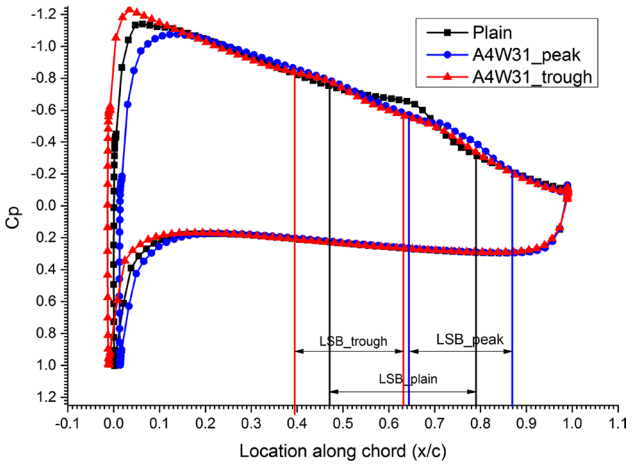

Fig. 16 C_p distribution over plain and tubercled airfoil A4W31

4.2.3 Numerical flow visualisation

Flow pattern over the airfoil is presented in this section to study how the tubercles alter the flow pattern and hence the airfoil performance. The results obtained at an AOA of 4° are presented in the section.

Surface flow visualisation over the plain and the tubercled airfoil A4W31 near the leading-edge is shown in Fig. 18. The streamlines are plotted on an offset surface, 0.01 mm above the airfoil surface. It can be observed that the flow near the airfoil leading-edge is divided into two parts about a bifurcation line, one part passes over the suction surface

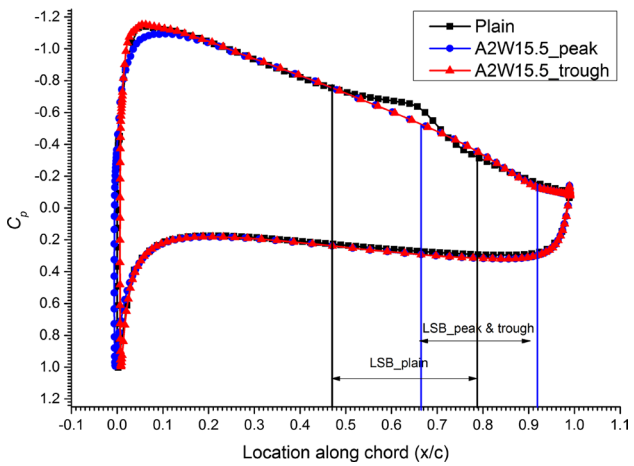

Fig. 15 C_p distribution over plain and tubercled airfoil A2W15.5

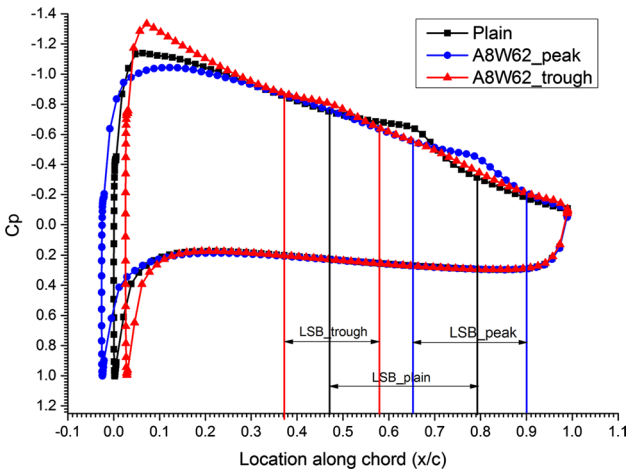

Fig. 17 C_p distribution over plain and tubercled airfoil A8W62

and the other over the pressure surface. For the plain airfoil, the flow after the bifurcation line goes straight towards the trailing edge (Fig. 18a) but for the tubercled one, it turns slightly to span-wise direction as seen in Fig. 18b.

This indicates that the tubercles modify the flow from the leading-edge itself by inducing some span-wise flow components. The flow is redirected as the flow approaches the leading-edge of the tubercled airfoil due to the waviness. The bulk of the flow is bunched together and flows towards the trough region as shown in Fig. 19, where the streamlines are coloured according to the velocity magnitude. For comparison purposes, the flow over the plain airfoil is shown in Fig. 19a, where the flow passes uniformly over the leading edge. The redirected flow gets accelerated in the trough evidenced by the red coloured streamlines as seen in Fig. 19b. Consequently, the pressure in the trough region is lower than that at the peak. This is depicted in the C_p plots shown in Figs. 15, 16 and 17, where the suction peak for the trough region lies above that for peak region of tubercled airfoil and plain airfoil.

Figure 20 illustrates the comparison of pressure contours on various tubercled airfoils and plain airfoil at the AOA of 4°. The plain airfoil has well-defined and constant pressure zones along the span-wise direction as seen in Fig. 20a. The pressure gradient is observed only in the stream-wise direction. In the case of the tubercled airfoils, a strong span-wise pressure gradient is established by the tubercles in a cyclic manner due to the accelerated flow through the trough. A low-pressure region is developed in the trough and a high-pressure region is formed over the peak. This pressure gradient is observed on all the tubercled airfoils and the region of influence increases with the increase in wavelength.

The flow has a tendency to turn span-wise from peak to trough driven by this cyclic pressure gradient, where the low-inertia near-wall fluid is drawn towards the low-pressure trough region from the peak as shown in Fig. 21. The tubercled airfoil with the lowest amplitude and wavelength has the least tendency for this movement (Fig. 21b), whereas the tendency increases with an increase in wavelength due to the larger low-pressure region as shown in Fig. 21c, d. The inclined flow further leads to complex flow structures with LSB and multiple three-dimensional vortices.

Streamline plot over the plain airfoil shows specific straight parting lines of separation (S) and reattachment (R)

Table 2 Location and size of LSB on plain and tubercled airfoils

Airfoil	Laminar separation bubble					
	Trough			Peak		
	Begin (x/c =)	End (x/c =)	Length (x/c)	Begin (x/c =)	End (x/c =)	Length (x/c)
Plain	0.48	0.79	0.31	0.48	0.79	0.31
A2W15.5	0.63	0.92	0.29	0.63	0.92	0.29
A4W31	0.39	0.63	0.24	0.65	0.87	0.22
A8W62	0.37	0.58	0.21	0.65	0.90	0.25

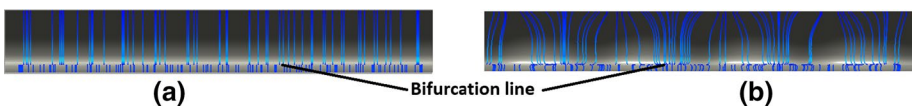

Fig. 18 Front view of the **a** plain airfoil and **b** tubercled airfoil-A4W31 with surface streamlines, showing the bifurcation line (streamlines are plotted on an offset surface at a distance of 0.01 mm from airfoil surface)

Fig. 19 Three-dimensional streamline over the airfoils

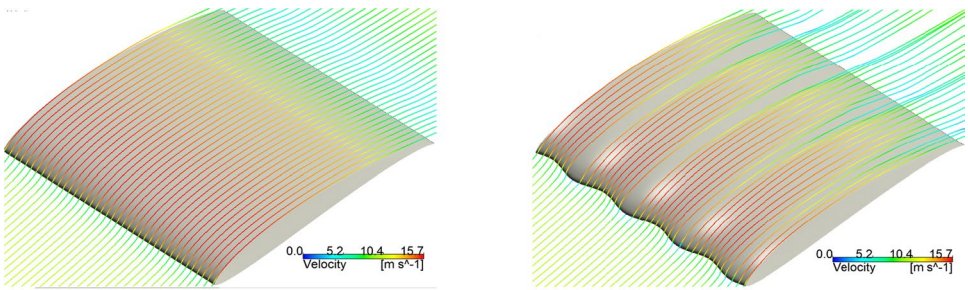

(a) plain airfoil **(b)** A4W31

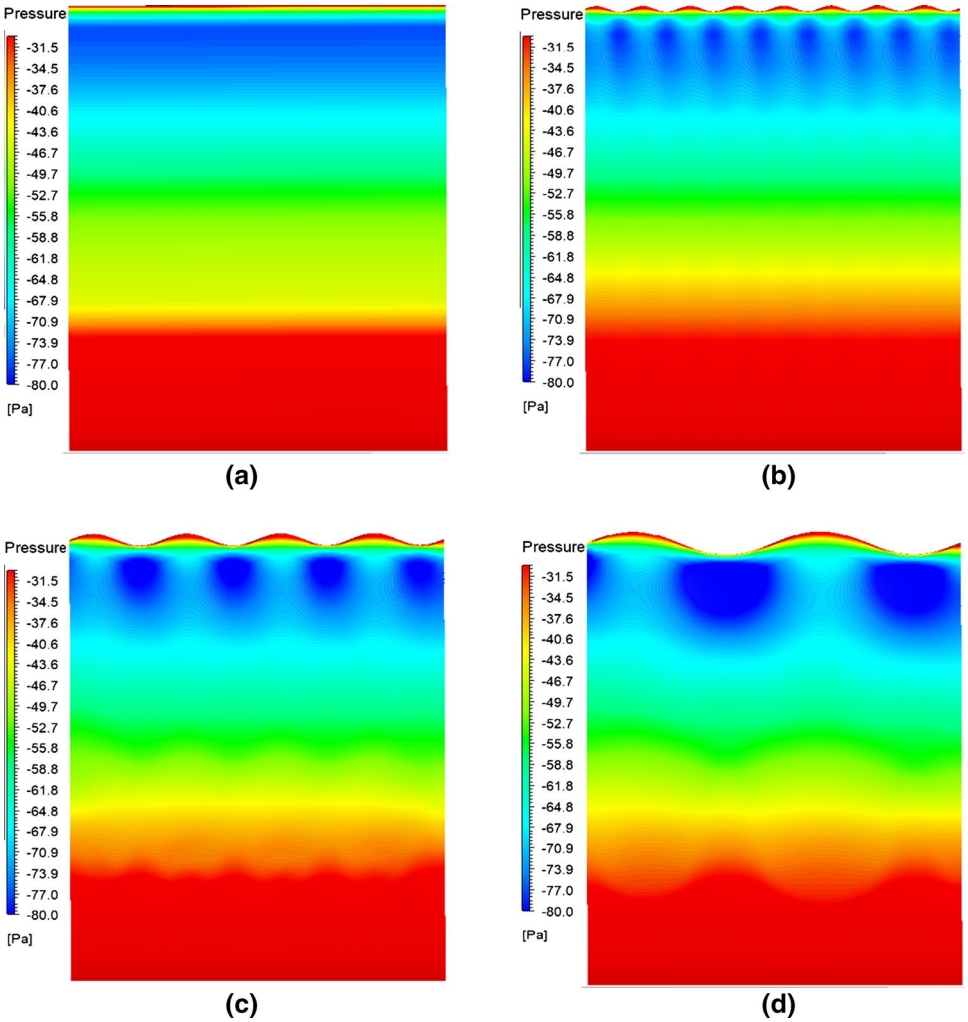

Fig. 20 Contours of pressure on the suction surface (top surface) at AOA = 4°: **a** plain and **c** A4W31 and **d** A8W62

as shown in Fig. 21, indicating the presence of LSB. For the tubercled airfoil A2W15.5, the flow pattern (Fig. 21b) is similar to the plain airfoil's (Fig. 21a), without any complex flow pattern and (unlike in the plain airfoil) the flow is attached throughout the airfoil length . There is no clear parting lines of separation or reattachment. This indicates that the airfoil modification with tubercles having amplitude 2 mm and wavelength 15.5 mm acted like a vortex generator and induced strong flow mixing. As a result, the flow got re-energised continued attached over the entire airfoil surface.

The A4W31 and A8W62 tubercled airfoils have complex flow structures as shown in Figs. 21c, d respectively. The surface flow pattern for both tubercled airfoils has a similar structure but differs in size. In order to analyse the surface flow pattern in detail, a view close to the suction surface of the tubercled airfoil A4W31 at an AOA 4° is shown in Fig. 22. As the flow moves downstream from the peaks of the tubercle, the span-wise flow components dominate and the streamline from the adjacent peaks move towards trough in between them. The streamlines form a pair of vortices (primary), rotate around the foci F1 and F2 as shown.

Flow separation from the airfoil surface first occurs at the point S1 along the trough marked in Fig. 22 and the separation is bounded by a parting line along the span-wise direction. The foci F1 and F2 lie inside the separation region (LSB). The separated flow reattaches at point R1 along the trough. After the formation of the primary vortices, part of the stream flows straight downstream, whereas the other part of the flow forms another pair of vortices behind the primary vortices called secondary vortices with foci F3 and F4. The secondary vortices are larger in size than the primary vortices. The stream moving straight downstream serves as a parting line between the vortices in both the pair of primary and secondary vortices and the stream does not participate in any of the vortex formation.

Along the peak, the secondary vortices serve as the reference for laminar separation. The region between the two consecutive secondary vortices, marked as points S2 and R2, serves as the separation and reattachment points. Since the separation points S1 and S2 as well as the reattachment

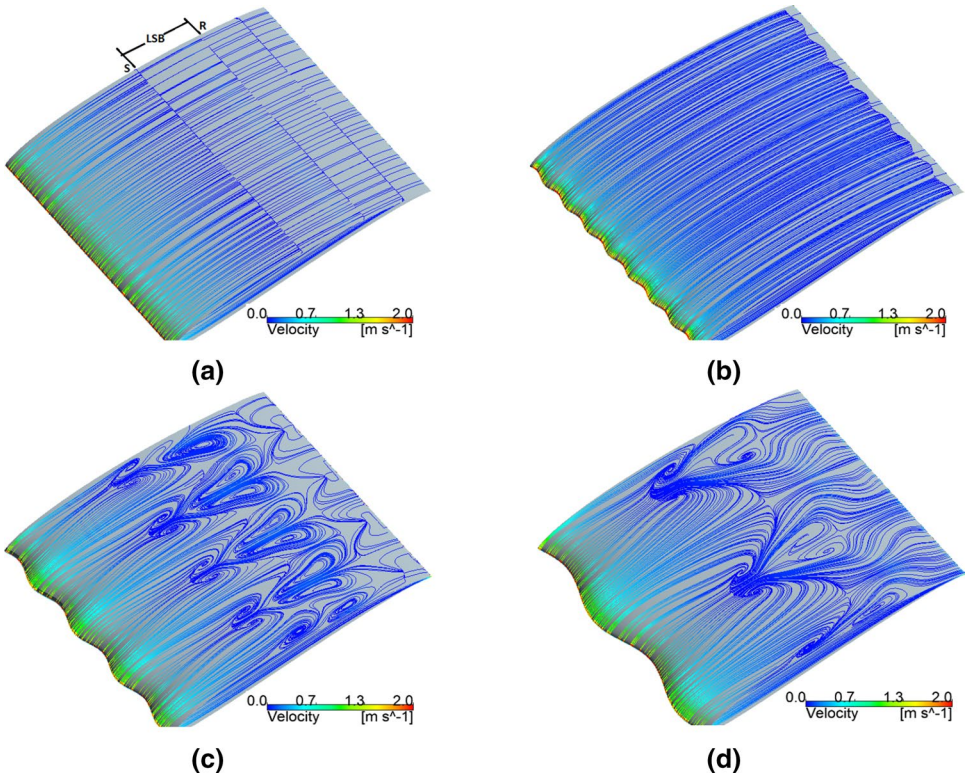

Fig. 21 Velocity streamlines on the suction side of the airfoil (offset surface) at AOA = 4°: **a** plain **b** A2W15.5, **c** A4W31 and **d** A8W62

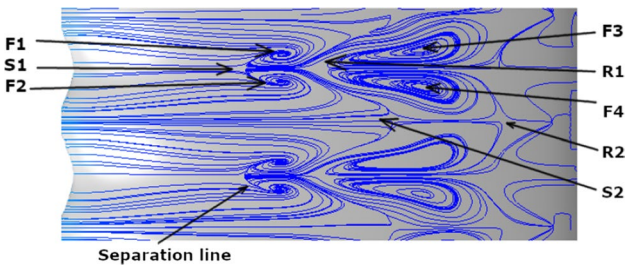

Fig. 22 Surface streamlines on A4W31 (offset surface) marked with different regions in the flow pattern at AOA = 4° (flow is from left to right)

points R1 and R2 are at different stream-wise locations, it can be inferred that the LSB forms in a sinusoidal manner, resembling the leading-edge of the airfoil.

The separation region is clearly identifiable in Fig. 23 where iso-surfaces of zero velocity are plotted over the airfoil surfaces. The thick blue region represents the separated flow. The plain airfoil has a well-defined region of LSB bounded with clear straight separation and reattachment lines along the span-wise direction as seen in Fig. 23a. Trailing edge (TE) separation also occurs in a straightforward manner. The A2W15.5 tubercled airfoil has no LSB formation as depicted previously. The A4W31 airfoil has a wavy laminar separation with clear separation and reattachment lines with wavy TE separation as shown in Fig. 23c. For the tubercled airfoil A8W62, due to the high amplitude of the tubercle, some portion of the laminar separation coalesce with TE separation as shown in Fig. 23d. The chord length of airfoil along the trough is smaller compared to the peak. This will result in a decrease of local Re at the trough, which promotes early separation of laminar flow compared to that in peak giving rise to a wavy LSB. The presence of stream-wise vortices enhances the boundary layer momentum exchange, which leads to reduced size of the LSB on tubercled airfoils compared to the plain airfoil.

To probe further details of the flow structure formation, three-dimensional behaviours of the flow are studied over the tubercled airfoil A4W31. The streamlines, after the primary vortex formation, are lifted away from the surfaces, join together and move downstream in a path between the secondary vortices as shown in Fig. 24. Since the flow initially participates in the primary vortex formation and then is lifted up, a thorough mixing of the flow with the higher-energy flow takes place. It results in higher energy for the separated fluid. The flow directly coming from the peak without any span-wise trend participates in secondary vortex formation. To further investigate the 3D flow structure over the airfoil, streamlines are plotted on multiple planes normal to the flow direction starting at $x/c = 0.35$ as shown in Fig. 25. The first plane is at the beginning of the primary vortex formation region where the flow separates from airfoil surface as seen in Fig. 25a. As the plane moves towards the trailing edge, the separation increases and starts forming 3D vortices as seen in Fig. 25b. A pair of clear 3D vortices

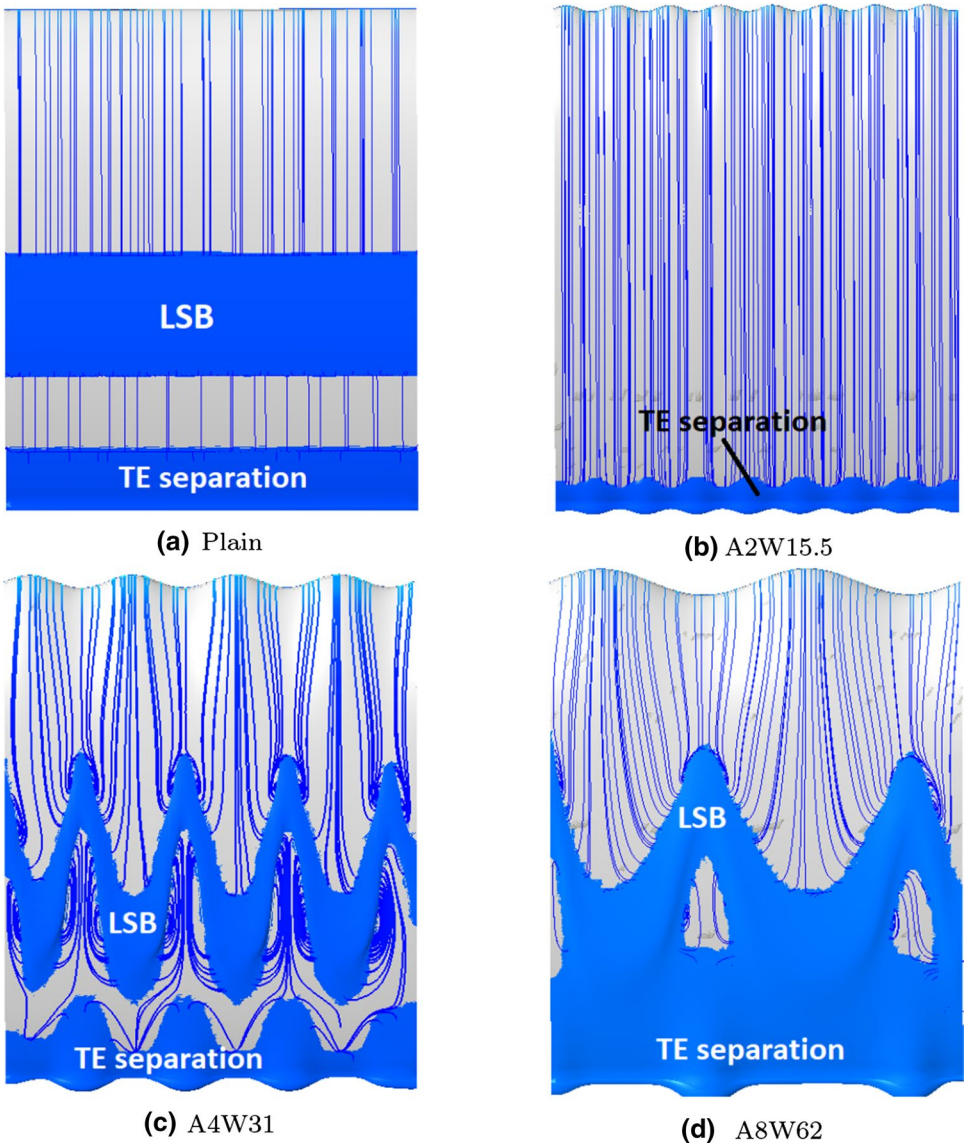

Fig. 23 Iso surface of zero velocity over the airfoils showing the region of separation (LSB) along with surface streamlines at AOA of 4° (continuous blue area shows the separation region and flow is from top to down)

are formed then (Fig. 25c) with foci F5 and F6, and these vortices themselves revolve around the foci F1 and F2 which is formed on the surface of the airfoil (Fig. 25d). Once it reaches the points F1 and F2, the flow rises up and mixes with mainstream flow.

4.2.4 Flow physics

It can be seen from Fig. 19 that, as the flow approaches the leading-edge of the airfoil with tubercle, the flow direction or streamline curvature changes suddenly resulting in reorganisation of span-wise vorticity into the transverse and stream-wise directions, generating stream-wise vorticity as seen in Fig. 25. This kind of vorticity is referred to as 'skew-induced' vorticity and the phenomenon is called Prandtl's secondary flow of the first kind [20]. These stream-wise vortices induce a high near-wall velocity gradient resulting in high shear stress. Such high shear stress results in additional skin friction drag and a net increase in total drag of the tubercled airfoils as seen in Fig. 13.

When the spacing between the tubercles is smaller (like tubercled airfoil A2W15.5), they act like a turbulence generator creating high boundary layer mixing. The flow becomes turbulent all over the airfoil with an attached boundary layer over the airfoil surface. This turbulent flow produces a detrimental effect on the performance as was found for vortex generator [10] resulting in a reduced performance of the tubercled airfoil even with the LSB elimination.

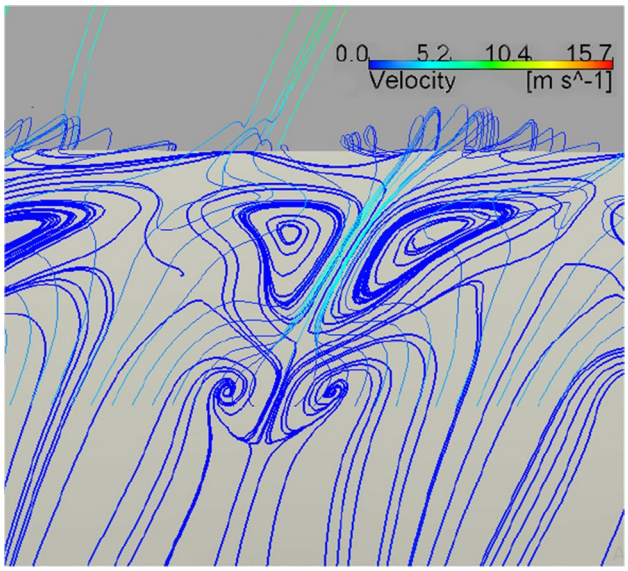

Fig. 24 Three-dimensional velocity streamlines emerging from the primary vortices (A4W31 at AOA = 4°)

5 Conclusions

Experimental and simulation studies were carried out to investigate the effect of leading-edge tubercles on the performance of low Re airfoil E216 at various AOA and Re of 100,000. The plain airfoil stalled at 12° AOA and the corresponding values of C_l and C_d are 1.37 and 0.081 as observed from the experimental results. Tubercled airfoils performed better in terms of C_l but exhibited higher C_d than plain airfoil. Highest improvement in C_l by 4.51% is observed in the experiment for the tubercled airfoil A8W62 at AOA of 6°. Other tubercled airfoils showed only negligible improvement in C_l. All tubercled airfoils have similar stall angle (of 12°, except for A2W15.5—which stalled at 10°) with lower C_{lmax} than the plain airfoil. The simulation results of the plain airfoil E216 are in good agreement with the wind tunnel experimental results. In the simulation, the plain airfoil stalled at 12° AOA with a maximum C_l value of 1.37 and C_d value of 0.069.

Surface pressure distribution and flow visualisation from the simulation reveal the presence of LSB on the plain

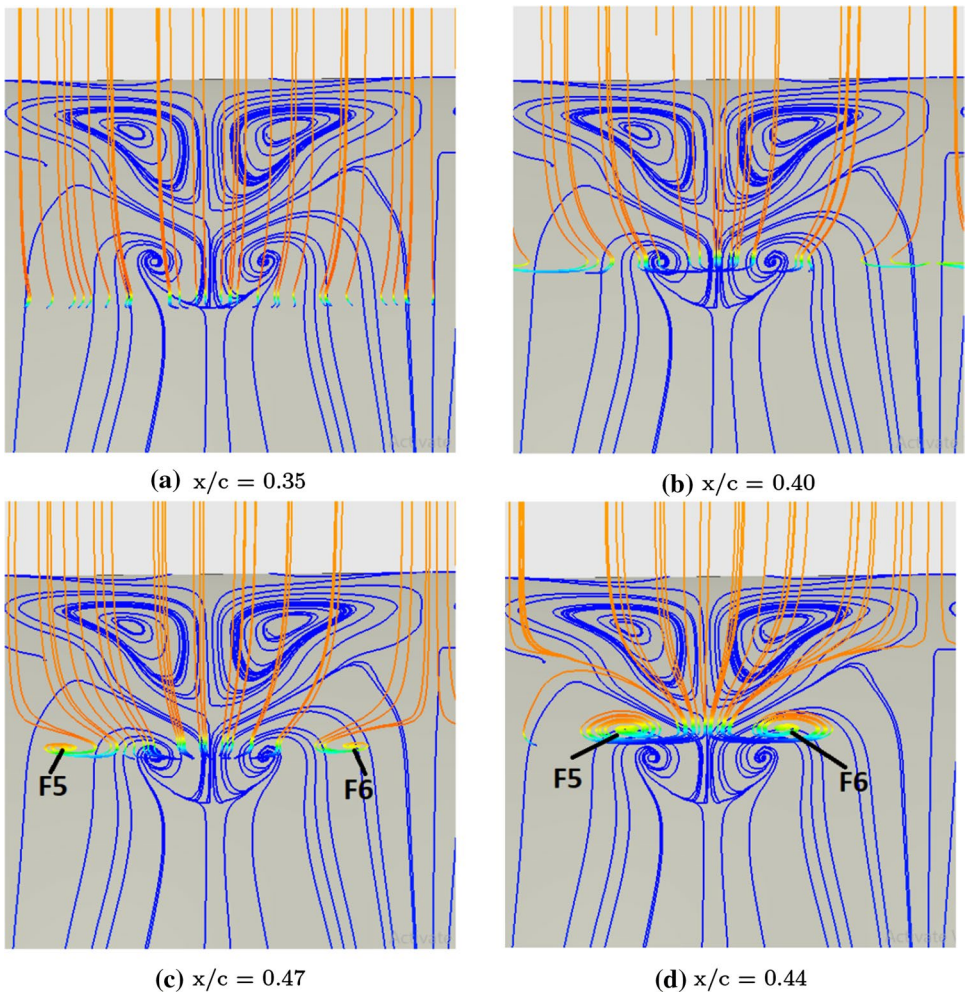

(a) x/c = 0.35 **(b)** x/c = 0.40

(c) x/c = 0.47 **(d)** x/c = 0.44

Fig. 25 Three-Dimensional vortex formation plotted on different planes normal to airfoil surface at different *x*/*c* distance starting from leading-edge of the tubercled airfoil A4W31 at AOA of 4°

airfoil. But in the tubercled airfoils A4W31 and A8W64, the LSB is re-oriented to form in a wavy manner, as opposed to the straight LSB in the case of plain airfoil. In the tubercled airfoil A2W15.5, LSB is formed in a straight manner due to the strong span-wise mixing of flow, where the tubercle acted like a vortex generator. For all other tubercled airfoils, the LSB along the trough is formed ahead of that at peak with a reduction in its mean length due to the high velocity along the trough due to the tunnelling effect in the flow over the trough. Cyclic variation of pressure distribution is observed from peak to peak near the leading-edge. This leads to the span-wise pressure gradient near to leading-edge generating a span-wise flow or flow inclination from peak to trough. Unlike previous studies instead of a single pair of vortex, two pairs of vortices are formed (namely primary and secondary vortices) which served as the separation point and reattainment point for LSB. It is observed that the pattern of surface streamlines varies with the combination of amplitude and wavelength of tubercles and there is no predictable general pattern for any particular combination.

The tubercles generate 3D stream-wise vortices apart from the surface vortices. These 3D vortices revolve around the foci of surface vortices. These 3D vortices induced additional turbulence resulting in higher drag generation. The source of span-wise vorticity generation is due to the 'skew-induced' vorticity and is Prandtl's secondary flow of the first kind.

Acknowledgements Authors would like to acknowledge the financial support extended by the Science and Engineering Research Board (SERB), India (Sanction order: EMR/2015/000879) to carry out this research work.

References

1. Bushnell DM, Moore K (1991) Drag reduction in nature. Annu Rev Fluid Mech 23(1):65–79
2. Cai C, Zuo Z, Liu S, Maeda T (2018) Effect of a single leading-edge protuberance on naca 634–021 airfoil performance. J Fluids Eng 140(2):021108
3. Chen T, Liou L (2011) Blockage corrections in wind tunnel tests of small horizontal-axis wind turbines. Exp Thermal Fluid Sci 35(3):565–569
4. Chishty MA, Parvez K, Ahmed S, Hamdani HR, Mushtaq A (2011) Transition prediction in low pressure turbine (LPT) using gamma theta model and passive control of separation. In: ASME 2011 international mechanical engineering congress and exposition, American Society of Mechanical Engineers Digital Collection, pp 193–200
5. Corsini A, Delibra G, Sheard AG (2013) On the role of leading-edge bumps in the control of stall onset in axial fan blades. J Fluids Eng 135(8):081104
6. Custodio D (2007) The effect of humpback whale-like leading edge protuberances on hydrofoil performance. Worcester Polytechnic Institute, Worcester
7. Favier J, Pinelli A, Piomelli U (2012) Control of the separated flow around an airfoil using a wavy leading edge inspired by humpback whale flippers. CR Mec 340(1–2):107–114
8. Fish FE, Battle JM (1995) Hydrodynamic design of the humpback whale flipper. J Morphol 225(1):51–60
9. FLUENT (2014) 15.0. theory guide
10. Godard G, Stanislas M (2006) Control of a decelerating boundary layer. part 1: optimization of passive vortex generators. Aerosp Sci Technol 10(3):181–191
11. Hansen KL (2012) Effect of leading edge tubercles on airfoil performance. PhD dissertation
12. Hansen KL, Kelso RM, Dally BB (2011) Performance variations of leading-edge tubercles for distinct airfoil profiles. AIAA J 49(1):185–194
13. Jahanmiri M (2011) Laminar separation bubble: its structure, dynamics and control. Techical report, Chalmers University of Technology
14. Johari H, Henoch CW, Custodio D, Levshin A (2007) Effects of leading-edge protuberances on airfoil performance. AIAA J 45(11):2634–2642
15. Kline SJ, McClintock F (1953) Describing uncertainties in single-sample experiments. Mech Eng 75(1):3–8
16. Menter F, Langtry R, Völker S (2006) Transition modelling for general purpose cfd codes. Flow Turbul Combust 77(1–4):277–303
17. Miklosovic D, Murray M, Howle L, Fish F (2004) Leading-edge tubercles delay stall on humpback whale (megaptera novaeangliae) flippers. Phys Fluids 16(5):L39–L42
18. Pedro HT, Kobayashi MH (2008) Numerical study of stall delay on humpback whale flippers. In: 46th AIAA aerospace sciences meeting and exhibit, vol 584, p 2008
19. Rist U, Augustin K (2006) Control of laminar separation bubbles using instability waves. AIAA J 44(10):2217
20. Rostamzadeh N, Hansen K, Kelso R, Dally B (2014) The formation mechanism and impact of streamwise vortices on naca 0021 airfoil's performance with undulating leading edge modification. Phys Fluids 26(10):107101
21. Russell J (1979) Length and bursting of separation bubbles: a physical interpretation. In: Science and technology of low speed motorless flight, vol 2085. NASA Conference Publication
22. Shah H, Mathew S, Lim CM (2014) A novel low reynolds number airfoil design for small horizontal axis wind turbines. Wind Eng 38(4):377–391
23. Shah H, Mathew S, Lim CM (2015) Numerical simulation of flow over an airfoil for small wind turbines using the γ-Re_θ model. Int J Energy Environ Eng 6(4):419–429
24. Skillen A, Revell A, Pinelli A, Piomelli U, Favier J (2014) Flow over a wing with leading-edge undulations. AIAA J 53(2):464–472
25. Sreejith BK, Sathyabhama A (2018) Numerical study on effect of boundary layer trips on aerodynamic performance of E216 airfoil. Eng Sci Technol Int J 21(1):77–88
26. Stanway MJ (2008) Hydrodynamic effects of leading-edge tubercles on control surfaces and in flapping foil propulsion. Ph.D. thesis, Massachusetts Institute of Technology
27. Van Nierop EA, Alben S, Brenner MP (2008) How bumps on whale flippers delay stall: an aerodynamic model. Phys Rev Lett 100(5):054502
28. Walker G (1992) The role of laminar-turbulent transition in gas turbine engines: a discussion. In: ASME 1992 international gas turbine and aeroengine congress and exposition. American Society of Mechanical Engineers, pp V001T01A108–V001T01A108